journal

J. Am. Ceram. Soc., 94 [S1] S42–S54 (2011)
DOI: 10.1111/j.1551-2916.2011.04503.x

The Design of Bonded Bimaterial Lattices that Combine Low Thermal Expansion with High Stiffness

Jonathan Berger,[†,‡] Chris Mercer,[§] Robert M. McMeeking,[‡,¶] and Anthony G. Evans[‡,¶]

[‡]Materials Department, University of California, Santa Barbara, California 93106

[§]Hybrid Materials Center, NIMS 1-2-1 Sengen, Tsukuba, Ibaraki 305 0047, Japan

[¶]Mechanical Engineering Department, University of California, Santa Barbara, California 93106

In engineered systems where thermal strains and stresses are limiting, the ability to tailor the thermal expansion of the constituent materials independently from other properties is desirable. It is possible to combine two materials and space in such a way that the net coefficient of thermal expansion (CTE) of the structure is significantly different from the constituents, including the possibility of zero and negative thermal expansion. Bimaterial lattices that combine low, negative, or an otherwise tailored CTE with high stiffness, when carefully designed, have theoretical properties that are unmatched by other known material systems. Of known lattice configurations with tailorable CTE, only one geometry, a pin-jointed lattice, has been shown to be stretch dominated and thus capable of having stiffness that approaches its theoretical upper bound. A related lattice with bonded joints, more amenable to fabrication, is developed that has a stiffness and CTE similar to the pinned structure. Analytical models for this rigid-jointed lattice's CTE and stiffness are developed and compared successfully with numerical results. A near space-filling, negative thermal expansion version of this lattice is devised and fabricated from titanium and aluminum. CTE measurements on this lattice are made and are well predicted by the analytical and numerical models. These insights guide the design of a family of bonded lattices with low areal density, low or negative CTE, and high stiffness to density ratio. Such lattices are shown to have a thermomechanical response that converges on pin-jointed behavior when the lattice elements are long and slender.

I. Introduction

Recent assessments have elucidated bimaterial, planar lattice concepts that attain zero (or low) thermal expansion coefficients (Fig. 1).[1–5] Among these, only the configuration depicted in Fig. 1(d) is known to combine low thermal expansion with high stiffness and strength. The lattice in Fig. 1(b) is the result of topology optimization and has biaxial stiffness near theoretical bounds, but has poor uniaxial stiffness, suffers from edge effects in lattices with limited periodicity, and has a complex geometry.[2] Furthermore, the lattice in Fig. 1(d), hereby known as the UCSB lattice, has properties that are transversely isotropic. Other stiff, strong, planar lattices have been identified that have zero, negative, or low thermal expansions in specific directions within its plane,[6] but are anisotropic, with significant thermal expansions in other in-plane orientations.

In the lattice of Fig. 1(d), the members that govern its response are defined within the unit cell depicted in Fig. 2. In this lattice, the outer, hexagonal (type I) members (length L_1 and width w_1) have the lower coefficient of thermal expansion (CTE) α_1, while the triangular, inner (type II) members (length L_2 and width w_2) have relatively higher CTE, α_2. At the nodal points A, J, F in the lattice (Fig. 2), the ratio of the effective thermal expansion $\bar{\alpha}$ to the CTE of the type I material α_1 is dictated by the constituent CTE ratio, $\lambda = \alpha_2/\alpha_1$, and by the skewness angle, θ, depicted in Fig. 2. For a pin-jointed lattice, the expansion coefficient, $\bar{\alpha}$ has been derived as[5]:

$$\frac{\bar{\alpha}}{\alpha_1} = \frac{1 - (1/2)\lambda \sin(2\theta)(1/\sqrt{3} + \tan\theta)}{1 - (1/2)\sin(2\theta)(1/\sqrt{3} + \tan\theta)} \quad (1)$$

For a representative material combination, Al alloy and Ti alloy, with $\lambda \approx 2.6$, zero expansion prevails for a pin-loaded lattice at skewness $\theta \approx 25°$.[5] When the lattices are bonded, or otherwise mechanically attached at the nodes to make them rigid joints, bending moments are introduced into the type I members and the thermal expansions are larger.[5]

To assess these predictions, lattices based on Ti and Al alloys have been made, and their thermal expansion characterized.[7] Measurements obtained for a pin-jointed unit cell are in close agreement with the prediction of Eq. (1). Those measured for lattices assembled using mechanical (dovetail) attachments, i.e. with rigid joints, give larger thermal expansions. A variety of features adversely affect the reliability and the repeatability of the thermal expansion of such rigid-jointed lattices: (i) local plastic strains induced by the thermal expansion difference between constituents at the bimaterial attachment. (ii) Bending moments associated with the reduction in effective member lengths due to member overlap at the nodal points where six type I members from three neighboring unit cells converge (Type J Node, Fig. 2). (iii) The reduction in effective length of type I members due to the intersection of struts at Type J and D nodes. (iv) The reduction in effective length of type I members due to material added at the dovetail bimaterial interface. A previous assessment has demonstrated that the detrimental effect of plasticity at the bimaterial attachment is minimal, because the plastic strains are highly localized, facilitating shakedown after the first few cycles.[7] Consequently, while the CTE mismatch at the attachment generates a nonlinear, hysteretic contribution to the thermal strain during the first cycle, the thermal expansion remains repeatable during all subsequent cycles. A preconditioning treatment is sufficient to initialize the system and stabilize the thermal expansion.

The detrimental influence of the nodal geometry on the bending moments is more substantive. The elevation in the bending stiffness of the type I members associated with nodes of Type J significantly increases the overall thermal expansion coefficient, as determined both experimentally and by finite-element (FE) analysis.[7] This detriment motivates a systematic

T. M. Pollock—contributing editor

Manuscript No. 28994. Received December 02, 2010; approved February 12, 2011.
This work was financially supported by the Office of Naval Research through the MURI program "Revolutionary Materials for Hypersonic Flight" (Contract N00014-05-1-0439).
[†]Author to whom correspondence should be addressed. e-mail: berger@engineering.ucsb.edu

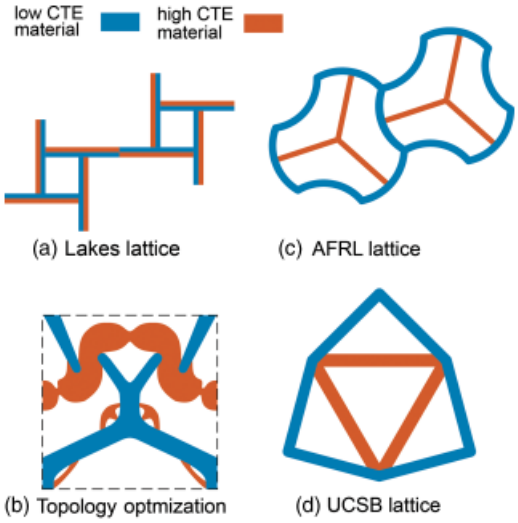

Fig. 1. Concepts for low thermal expansion lattices; (a) the Lakes lattice[1]; (b) the lattice obtained by topology optimization[2,3]; (c) the AFRL design[4]; and (d) the UCSB lattice.[5]

study that seeks geometrically straightforward configurations, amenable to manufacture, that impart thermal expansion closer to the pin-jointed prediction of Eq. (1), while retaining high stiffness and strength. The objective of this article is to seek such configurations, but with a focus, for the time-being, on stiffness.

The thermal expansion characteristics to be pursued emphasize designs that reduce the bending moments in the slender type I members. Analytic results are presented in Section II for the original design and extended to an alternative, offset design (Fig. 3). The alternative design is comprehensively analyzed in Section III by the FE method and specific designs discussed. It will be demonstrated that bonded, offset configurations can be conceived that have thermal expansions essentially the same as the pin-jointed lattice. Given the minimal-member bending stiffness for these new lattices, basic elasticity results are derived for pin-jointed systems in Section IV. These specify the salient trends in elastic response. Thereafter, a series of FE results for rigid-jointed systems are generated to ascertain deviations in stiffness from pin-joint predictions.

II. Design Principles for Low Thermal Expansion

Predicated on the foregoing assessment that the thermal expansions in excess of the pin-jointed lattice are primarily affected by the bending moments in the type I members, a beam theory methodology has been devised that identifies geometrically straightforward designs that converge to pin-jointed behavior. Two design layouts are considered: (i) One conforms to Fig. 2, with the effective rigidity of the material around the joints taken into account. (ii) The other allows the unit cells to be separated by spacers (Fig. 3), both relaxing the joint rigidity limitation and permitting greater motions of type I members. The latter feature allows the implementation of a unit cell with a negative thermal expansion, so that, when averaged with the positive expansion of the spacer, the lattice has a zero or extremely low CTE. The joints are represented as circular flanges (Fig. 2), having radius R_1 (for Type A, F, and J) and radius R_2 (for Type B, C, and D). The radius R_1 is defined as the convergence of struts of type AD and CJ, and R_2 by the convergence of struts of type AD with type BD and CD. The rigidity of the flanges reduces the effective length of the adjacent struts.

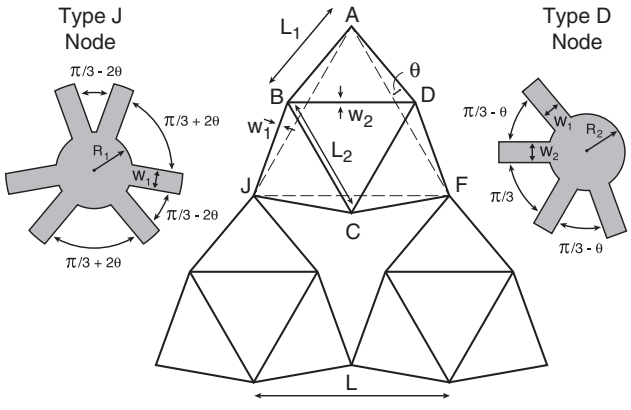

Fig. 2. Unit cell and joint geometry.

By considering the incremental changes in member length during thermal expansion, and eliminating the increment of θ, we find for the original design of Fig. 2

$$\frac{\Delta L}{L} = \frac{\sqrt{3}\frac{\Delta L_1}{L_1} - \sin\theta(\cos\theta + \sqrt{3}\sin\theta)\frac{\Delta L_2}{L_2}}{\cos\theta(\sqrt{3}\cos\theta - \sin\theta)} \tag{2}$$

where

$$L_1 = \frac{L}{2\cos\theta} \tag{3}$$

$$L_2 = \frac{L}{2}(1 + \sqrt{3}\tan\theta) \tag{4}$$

and the symbol Δ followed by the letter L, with or without subscripts, indicates change of length. Because type II struts do not bend, but sustain only an axial load T_2, their strain is

$$\frac{\Delta L_2}{L_2} = \left(\frac{T_2}{E_2 A_2} + \varepsilon_2^t\right)\left(1 - 2\frac{R_2}{L_2}\right) + 2\hat{\varepsilon}_2^t\frac{R_2}{L_2} \tag{5}$$

where E_2 is Young's modulus for type II members, A_2 is their cross-sectional area, ε_2^t is the thermal strain in the struts and $\hat{\varepsilon}_2^t$ is the effective thermal strain of joints of type D. Type I struts bend and stretch, and their axial strain is given by

$$\frac{\Delta L_1}{L_1} = \left(\frac{T_1}{E_1 A_1} + \varepsilon_1^t\right)\left(1 - \frac{R_1 + R_2}{L_1}\right) + \hat{\varepsilon}_1^t\frac{R_1}{L_1} + \hat{\varepsilon}_2^t\frac{R_2}{L_1} \tag{6}$$

where T_1 is the tension in these members, E_1 is Young's modulus for type I members, A_1 is their cross-sectional area, ε_1^t their thermal strain and $\hat{\varepsilon}_1^t$ is the effective thermal strain of joints of type J.

Type I struts sustain a uniform shear force V and a nonuniform bending moment M (Fig. 4). Equilibrium at joints A and D requires that

$$T_1 = \frac{\cos\theta + \sqrt{3}\sin\theta}{\sqrt{3}\cos\theta - \sin\theta}V \tag{7}$$

and

$$T_2 = -\frac{2}{\sqrt{3}\cos\theta - \sin\theta}V \tag{8}$$

Inspection of Fig. 2 reveals that, by geometry, the transverse bending deflection of AD is given by

$$\delta = L_1\Delta\theta = \frac{\Delta L_2 - (\cos\theta + \sqrt{3}\sin\theta)\Delta L_1}{\sqrt{3}\cos\theta - \sin\theta} \tag{9}$$

while Euler–Bernoulli beam theory gives

$$\delta = \frac{V(L_1 - R_1 - R_2)^3}{12E_1 I_1} \tag{10}$$

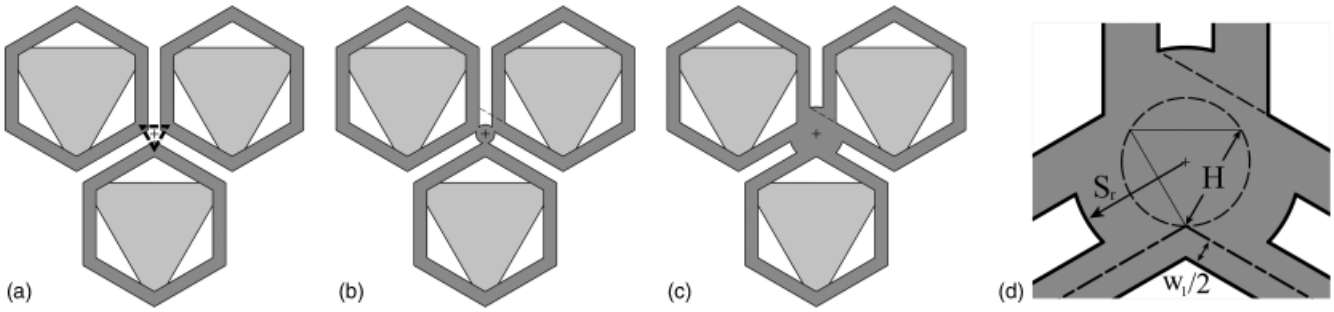

Fig. 3. Spaced lattices with $\theta = \pi/6$, with no additional material (a), undersized stiffener (b), and appropriately sized spacer (c and d) where axial member loads can be transmitted directly to adjacent unit cells. Spacer has characteristic dimension H while the stiffener has radius S_r.

where I_1, for type I members, is the second moment of area of the cross section about the neutral axis, so that $E_1 I_1$ is the bending stiffness of type I members, specified for bending in the plane of the lattice. Elimination of δ and V among Eqs. (7)–(10) provides

$$T_1 = \frac{12E_1I_1L_1(\cos\theta+\sqrt{3}\sin\theta)^2\left(\frac{\Delta L_2}{L_2}-\frac{\Delta L_1}{L_1}\right)}{(L_1-R_1-R_2)^3(\sqrt{3}\cos\theta-\sin\theta)^2} \tag{11}$$

and

$$T_2 = \frac{24E_1I_1L_1(\cos\theta+\sqrt{3}\sin\theta)\left(\frac{\Delta L_2}{L_2}-\frac{\Delta L_1}{L_1}\right)}{(L_1-R_1-R_2)^3(\sqrt{3}\cos\theta-\sin\theta)^2} \tag{12}$$

Use of Eqs. (5) and (6) allows a solution for the strut tensions as

$$T_1 = \frac{12E_1I_1L_1(\cos\theta+\sqrt{3}\sin\theta)^2\left(\varepsilon_2^t\frac{\hat{L}_2}{L_2}+2\hat{\varepsilon}_2^t\frac{R_2}{L_2}-\varepsilon_1^t\frac{\hat{L}_1}{L_1}-\hat{\varepsilon}_1^t\frac{R_1}{L_1}-\hat{\varepsilon}_2^t\frac{R_2}{L_1}\right)}{\hat{L}_1^3\left\{(\sqrt{3}\cos\theta-\sin\theta)^2+\frac{12I_1}{A_1\hat{L}_1^2}\left[\frac{2E_1A_1\hat{L}_2}{E_2A_2\hat{L}_1}+(\cos\theta+\sqrt{3}\sin\theta)^2\right]\right\}} \tag{13}$$

and

$$T_1 = \frac{24E_1I_1L_1(\cos\theta+\sqrt{3}\sin\theta)\left(\varepsilon_2^t\frac{\hat{L}_2}{L_2}+2\hat{\varepsilon}_2^t\frac{R_2}{L_2}-\varepsilon_1^t\frac{\hat{L}_1}{L_1}-\hat{\varepsilon}_1^t\frac{R_1}{L_1}-\hat{\varepsilon}_2^t\frac{R_2}{L_1}\right)}{\hat{L}_1^3\left\{(\sqrt{3}\cos\theta-\sin\theta)^2+\frac{12I_1}{A_1\hat{L}_1^2}\left[\frac{2E_1A_1\hat{L}_2}{E_2A_2\hat{L}_1}+(\cos\theta+\sqrt{3}\sin\theta)^2\right]\right\}} \tag{14}$$

where the notation

$$\hat{L}_1 = L_1 - R_1 - R_2 \tag{15}$$

and

$$\hat{L}_2 = L_2 - 2R_2 \tag{16}$$

has been introduced. When these results are inserted into Eqs. (5) and (6) and the outcome used in Eq. (4), the thermal expansion of the lattice becomes

$$\frac{\Delta L}{L} = \frac{\sqrt{3}\left(\varepsilon_1^t\frac{\hat{L}_1}{L_1}+\hat{\varepsilon}_1^t\frac{R_1}{L_1}=\hat{\varepsilon}_2^t\frac{R_2}{L_1}\right)-(\cos\theta+\sqrt{3}\sin\theta)\sin\theta\left(\varepsilon_2^t\frac{\hat{L}_2}{L_2}+2\hat{\varepsilon}_2^t\frac{R_2}{L_2}\right)}{(\sqrt{3}\cos\theta-\sin\theta)\cos\theta} + \frac{12I_1(\cos\theta+\sqrt{3}\sin\theta)\left[\sqrt{3}\cos\theta+\left(3+\frac{2E_1A_1\hat{L}_2}{E_2A_2\hat{L}_1}\right)\sin\theta\right]\left(\varepsilon_2^t\frac{\hat{L}_2}{L_2}+2\hat{\varepsilon}_2^t\frac{R_2}{L_2}-\varepsilon_1^t\frac{\hat{L}_1}{L_1}-\hat{\varepsilon}_1^t\frac{R_1}{L_1}-\hat{\varepsilon}_2^t\frac{R_2}{L_1}\right)}{A_1\hat{L}_1^2(\sqrt{3}\cos\theta-\sin\theta)\cos\theta\left\{(\sqrt{3}\cos\theta-\sin\theta)^2+\frac{12I_1}{A_1L_1^2}\left[\frac{2E_1A_1\hat{L}_2}{E_2A_2\hat{L}_1}+(\cos\theta+\sqrt{3}\sin\theta)^2\right]\right\}} \tag{17}$$

When the bending stiffness is negligible ($I_1 = 0$), and the joint radii R_1 and R_2 are neglected, this result simplifies to Eq. (1).

The result in Eq. (17) highlights the two effects of bonded joints. The first involves the finite extent of the joints (R_1 and R_2 are nonzero), implied by the first term on the right hand side. The second arises because the bending of type I struts adds strain to the thermal response, signified by the second term on the right hand side.

Appropriate choices for the joint radii (Fig. 2) are

$$R_1 = \frac{3w_1}{\pi - 6\theta} \tag{18}$$

and

$$R_2 = \max\left(\frac{3(w_1+w_2)}{2\pi-6\theta}, \frac{3w_2}{\pi}\right) \tag{19}$$

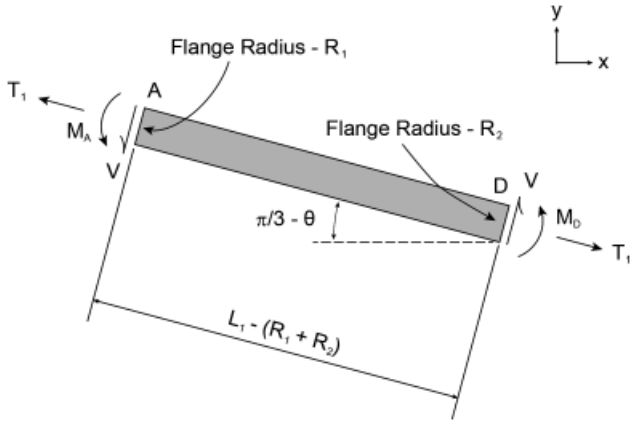

Fig. 4. Type I members sustain an axial load, T, shear, V, and bending moment, M.

The thermal expansion for nodes A, J, F is

$$\hat{\varepsilon}_1^t = \varepsilon_1^t \tag{20}$$

An appropriate choice for nodes B, C, D is a weighted average of the expansion of type I and II materials,

$$\hat{\varepsilon}_2^t = \frac{1}{3}(2\varepsilon_1^t + \varepsilon_2^t) \tag{21}$$

Results for the linear thermal expansion for various material combinations are plotted against θ in Fig. 5, with a range of values for the bending stiffness parameter $I_1/A_1L_1^2$used for illustration.

The above results affirm that the design of joints of Type A, J, F is critical to the realization of low thermal expansion behavior, because the low angle included between type I members from adjacent unit cells leads to excessively large R_1. This limitation is obviated by using an offset design wherein the centers of neighboring unit cells are displaced, allowing R_1 to become small even when $\theta \to \pi/6$. Such offset designs are achieved by insertion of a spacer made from type I material, as shown in Fig. 3. The spacer removes the coupling of $\hat{L}_1$ and θ, for a fixed L, enabling the use of larger values of θ. Offset designs can have negligible bending, whereupon, the thermal expansion can be closely approximated by the first term on the right hand side of Eq. (17), with R_1 and R_2 neglected. The CTE for the offset lattice is thus

$$\frac{\bar{\alpha}}{\alpha_1} = \frac{\sqrt{3} - \lambda F(\theta)}{\sqrt{3} - F(\theta)} \left(\frac{L}{L + \mathrm{H}}\right) + \frac{\mathrm{H}}{L + \mathrm{H}} \tag{22}$$

where H is the size of the spacer and $F(\theta) = (\cos\theta + \sqrt{3}\sin\theta)\sin\theta$. When H is zero, Eq. (1) is recovered once more. The formula in Eq. (22) can be used to guide low thermal expansion lattice designs; specifically, Eq. (22) predicts that zero thermal expansion of the lattice occurs when

$$\frac{\mathrm{H}}{L} = \frac{\lambda F(\theta) - \sqrt{3}}{\sqrt{3} - F(\theta)} \tag{23}$$

This design has unit cells that contract upon heating, compensating for the expansion of the spacers. Such solutions are feasible when $\sqrt{3}/\lambda < F(\theta) < \sqrt{3}$(note that, within this range, the unit cell has negative thermal expansion). The upper limit of this range coincides with $\theta = \pi/3$. For illustration, when $\lambda = 2$, the lower limit is $\theta = \pi/6$. Beyond these limits is the requirement that joints A, J, F remain physically small, requiring that $\frac{\geq H\sqrt{3}w_1 \sin\theta}{F(\theta)}$, whereupon the type I elements from neighboring unit cells have no intersection. From Eq. (23), this requirement provides

$$\frac{w_1}{L} \leq \frac{[\lambda F(\theta) - \sqrt{3}]F(\theta)}{[\sqrt{3} - F(\theta)]\sqrt{3}\sin\theta} \tag{24}$$

revealing that the slenderness of type I elements has to be respected. Consequently, when $\theta = \pi/6$, Eq. (24) gives $w_1/L \leq (\lambda - 2)$, indicating that the design can be satisfied provided that $\lambda = \alpha_2/\alpha_1 > 2$, ensuring that w_1 is positive. Moreover, any material combination with λ slightly in excess of 2 (say more than 2.1) is acceptable, because w_1/L must be small to ensure low bending stiffness.

Alternatively, Eq. (24) can be recast as a condition on θ with λ and w_1/L already selected. The outcome is not transparent because it involves a combination of trigonometric functions of θ without obvious simplification. Nevertheless, inspection indicates that any θ slightly above the lower limit $F(\theta) = \sqrt{3}/\lambda$ will satisfy Eq. (24). Specific cases should be assessed numerically to ensure a satisfactory design, as elaborated below.

A chosen design is limited in its range of temperature operation by the requirement that the triangle of type II elements has space into which material can expand when the lattice is heated. The critical condition occurs when joint C (Fig. 2) touches its counterparts from the two adjacent unit cells. It is straightforward to ascertain that the strain increment in type II bars that causes this critical condition is

$$\varepsilon_2^t = \frac{\cos\theta - \sqrt{3}\sin\theta + \frac{2\mathrm{H}}{L}\cos\theta}{\cos\theta + \sqrt{3}\sin\theta} \tag{25}$$

Consequently, the operating temperature range must be chosen to ensure that thermal straining of type II elements is smaller. For $\theta \sim \pi/6$ and greater a careful choice of $\frac{\mathrm{H}}{L}$ is needed, because $\cos\theta - \sqrt{3}\sin\theta \leq 0$ for $\theta \geq \pi/6$.

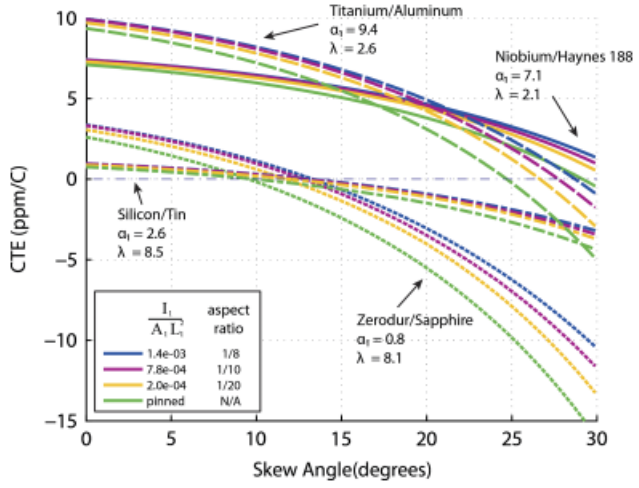

Fig. 5. Lattice coefficient of thermal expansion as a function of skew angle θ and type I member aspect ratios.

III. Specific, Low Expansion, Offset Designs

(1) FE Method

Lattices are modeled using a representative volume element (RVE) FE technique. Three-dimensional models are subject to periodic boundary conditions for the two in-plane dimensions in the form of uniform macroscopic strains. The relative displacements between pairs of boundary nodes are controlled by tying their displacements together consistent with the strains we wish to impose.[8,9] The third, z-direction, is left free. A single node on the interior of the model is held fixed in space to prevent rigid-body translations. The commercial FE code ABAQUS[10] is used for mesh generation and to perform analysis. MATLAB[11] code is used extensively to manipulate meshes, apply boundary conditions, and for postprocessing. Periodic boundary conditions were implemented in Cartesian coordinates. A typical RVE is pictured in Fig. 6. Typical meshes consist of ~20 000 to ~70 000 eight-noded linear hexahedral elements (type C3D8R). The number of elements varies greatly with the relative density of the lattice geometry being analyzed, which ranged from 8% to 98% for slender to space-filling designs, respectively. Mesh sensitivity is studied to ascertain model resolution at which solutions converge. Because the average strains are small, there is no distinction between the macroscopic Cauchy stress and the macroscopic nominal stress, so that the macroscopic stress can be computed by simply dividing force resultants by section areas for the undeformed volume of the RVE.

(2) Offset Lattices

In stretch-dominated structures, where loads are well distributed, stress contours are rather uniform, and consequently the structure is relatively efficient in its utilization of material. On the other hand, FE calculated thermomechanical stress distributions in the original lattice design reveal large nonuniform

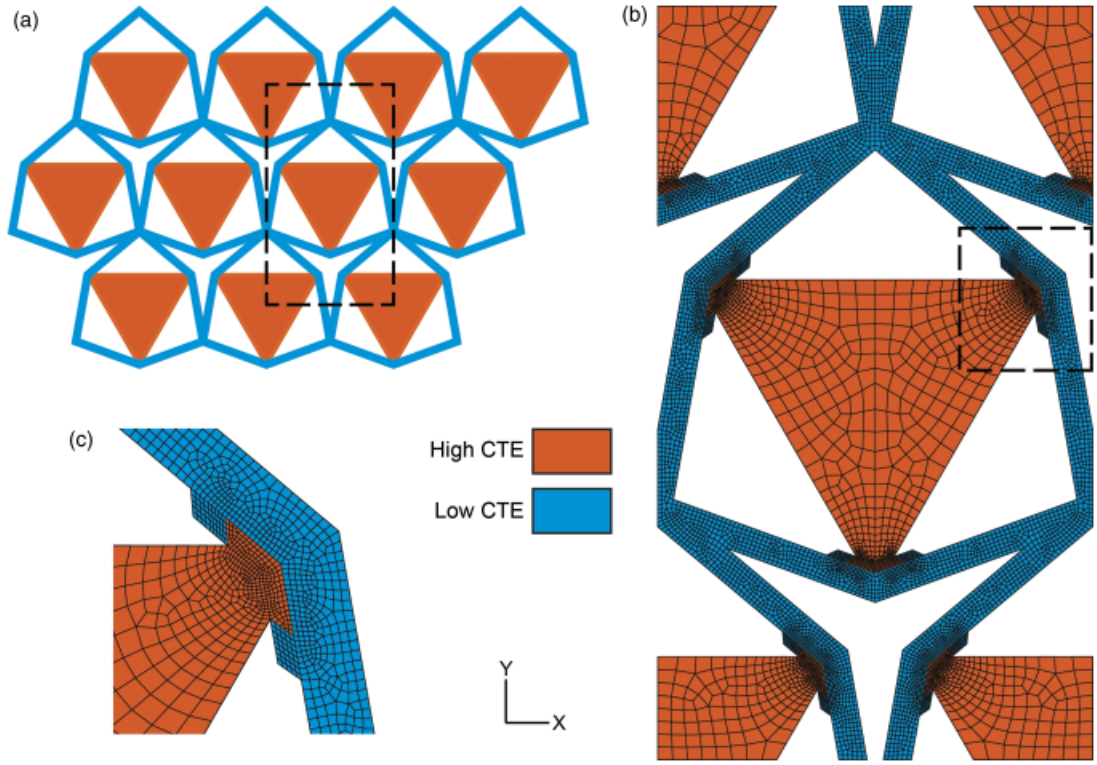

Fig. 6. (a) Perimeter of unit cell used for computations. (b) Representative finite-element mesh that consisted of 50 000–70 000 three-dimensional elements. (c) Detail of a bimaterial joint region.

bending stresses associated with rigidity and member intersection at the joints (Fig. 7(a)). The lattices analyzed to obtain these results are modeled with the temperature-dependent properties of Ti and Al alloys listed in Table Ib and subject to a temperature excursion from 40° to 250°C. The bimaterial interface, in reality press-fit, is considered to be perfectly bonded for simplicity. Simulations that model the interface between sublattices with contact in compression, and a frictional coefficient of $\mu = 1$, give results that are negligibly different from welded models.

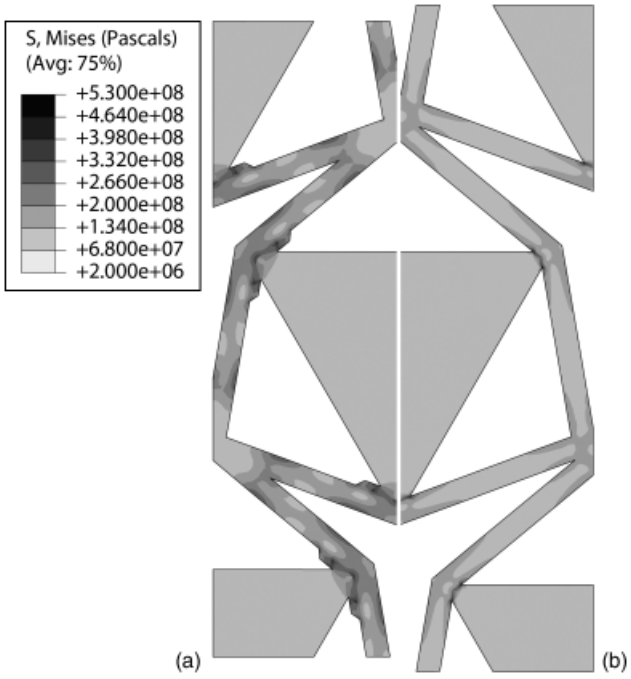

Fig. 7. Finite-element thermomechanical stress distribution in Ti and Al lattices given the material properties listed in Table I and subject to a 175°C temperature excursion—(a) original design and (b) new offset design.

The maximum tensile equivalent stress (also known as the von Mises stress) is located in the bimaterial joint region and results from CTE mismatch between constituents. In the temperature range analyzed, the maximum tensile equivalent stress is lower than the tensile yield stress in both materials.

Constraints on the motion of the lattice's components drive the macroscopic CTE toward that of the constituents. By placing a spacer (Fig. 3), with characteristic dimension H, between unit cells and eliminating excess material around the bimaterial joint, the lattice geometry can be designed so that it behaves according to the original concept for low CTE, i.e. with negligible stress (Fig. 7(b)). Contours for the revised design show greatly reduced bending stresses and the overall lattice behavior is in good agreement with new analytical predictions (Fig. 8).

Table Ia. Temperature Average Values of Material Properties—For the Range 40°–215°C

		Coefficient of thermal expansion (ppm/°C)	Young's modulus (GPa)	σ_y (MPa)
Type-1 material	Ti–6Al–4V	9.4	110	800
Type-2 material	7075-T6 aluminum	24.3	70	400

Table Ib. Temperature-Dependent Material Properties

		Coefficient of thermal expansion (ppm/°C)	Young's modulus (GPa)	σ_y (MPa)	Temperature (°C)
Type-1 material	Ti–6Al–4V	9.2	110	1100	20
		9.6		858	300
Type-2 material	7075-T6	22.9	70	434	20
		26.3		391	200
				339	300

(3) Lattice Design

For any pair of constituent materials and their associated properties, there is a range of skew angles, θ, over which a desired lattice CTE can be achieved. Properties such as stiffness, the Poisson ratio, and strength vary over this range so that any one solution may be superior to others depending on design requirements. For a unit temperature change, $\Delta T = 1$ so that $\varepsilon_i^t = \alpha_i$, Eq. (17) gives the thermal expansion coefficient of the lattice and can be inserted into Eq. (26),

$$\bar{\alpha} = \frac{\Delta L + \mathrm{H}\alpha_1}{L + \mathrm{H}} \tag{26}$$

to calculate the expansion of a spaced lattice. The macroscopic thermal strain in a spaced lattice is the weighted sum of the lattice and spacer strain, the latter having thermal expansion coefficient α_1. Equation (26) can be used to identify regions of design parameter space where lattices with the desired thermomechanical response exist. Designs in this neighborhood can then be investigated through FE to address specific geometries and to investigate their thermomechanical response in comparison with the results in Section II.

The thermomechanical strain response of the bimaterial joints in Eq. (21) is assumed to be an average of the constituents. While this approximation is sufficient for exploratory investigations, specific mechanical bimaterial interface geometries must be considered when designing real structures, as their behavior may differ substantially from this idealization. The dovetail joints used by Steeves *et al.*,[5,7] and in the current effort, are examples of bimaterial attachments. Mechanical connections capable of carrying tensile loads are necessary for transmitting all applied macroscopic loading situations except biaxial tension. The size of these joints, given by their characteristic dimension, R_2, reduce the effective length of members ($\hat{L}_1$ and $\hat{L}_2$, Eqs. (15) and (16)).

For fixed values of w_1 and w_2, the thermomechanical response of the system is a strong function of the member effective lengths, and therefore of R_1 and R_2. In many designs, a single radius R_2 does not exist by which both type I and II members are reduced equally at the Type D joints (Eqs. (15) and (16)). The actual reduction in effective length of members at these nodes is a function of member width and the relative angle at which they are incident to the joint. To identify designs with a tailored and well-predicted CTE, which is amenable to fabrication, more detailed modeling is necessary.

The addition of the spacer (Fig. 3) allows practical access to previously unachievable skew angles and corresponding higher relative densities. In previous designs without the spacer, at skew angles approaching 30°, members from adjacent unit cells intersect to an extent, and prevent the desired thermomechanical response, and the desired CTE cannot be realized. A skew angle of 30°, without a spacer present, results in type I members in adjacent cells being parallel and a hexagonal unit cell appearance. If only the area bounded by the unit cell is considered, these designs can achieve near-maximum areal density as an assembly of hexagonal cells with small gaps between them. The size of the gaps between unit cells is directly related to the size of the spacer H. Upon temperature excursion from the reference state, type I members expand, distort, and rotate, causing Type D nodes to translate away from the center of the unit cell. The size of the spacer and the corresponding gap is dictated by the maximum outward deflection of these nodes in the specified temperature range while considering the need to avoid adjacent unit cells impinging upon each other after thermal straining. For some designs with skew angles near or above 30°, an upper use temperature exists at which initially nearly parallel type I members in adjacent cells deform to contact each other causing the lattice to densify. For these designs, the upper use temperature can be increased by expanding the size of the spacer at the cost of driving the CTE of the system toward that of the type I material (Eq. (26)). Densification may also significantly influence the stiffness and strength of these lattices and may be a beneficial feature in some applications. If material continuity is beneficial, such as for aerodynamic surfaces, densified lattices can be useful.

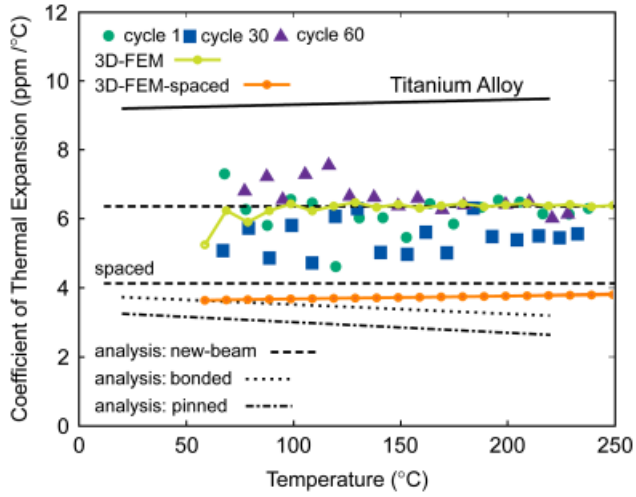

Fig. 8. Comparison of results from finite-element analysis for coefficient of thermal expansion and experiment.

In some spaced lattice designs where the dimension of the spacer is on the order of w_1, no additional material is needed to achieve this offset. In others, designs with skew angles in the neighborhood of 30°, unit cells may intersect minimally or not at all (Fig. 3) and the strength and stiffness joint will suffer. A disk of material centered on the spacer, a stiffener with radius S_r can be added to the lattice to maintain continuity and transmit stresses between unit cells. If the disk of material is too small, stress concentrations in these regions can be design limiting. An appropriate radius for this disk is one where axial loads in type I members can be directly transmitted to adjacent cells (Figs. 3(c) and (d)). This stiffener has a dimension independent of the spacer and may be useful in facilitating a connection between the lattice and a substructure.

As type II members are not subject to thermally induced bending stresses, members with geometries other than truss or beam-like forms can be considered without altering the mechanics of the system.[5] In Fig. 10, the lattices pictured in the middle and on the right (b and c) are variations of the lattice on the left (a) incorporating type II members that are not simple prismatic beams. Stiffening of type II members drives the thermal expansion of the system to lower values. The increased stiffness of these members can be modeled by using an effective modulus E_2^* for E_2 in Eqs. (13) and (14). The only restriction in geometry is that the type II members not impinge on, and reduce the effective length of the slender type I members when thermomechanically strained. Previous fabricated designs have used truss and solid triangular inner type II members (Figs. 9(a) and (b)).[5,7] To explore the potential space-filling properties of this lattice, a hexagonally shaped type II sublattice geometry was chosen for fabrication in this work.

If in-plane geometries of members are specified to have a finite width centered on the lines shown in Fig. 2, the width of the bimaterial joint is limited by the width of type II members, w_2 (for the geometry considered in this work). Selecting a small bimaterial joint resulted in a small value of w_2 in Eq. (17). To account for the much larger cross section of the hexagonal geometry used, an effective modulus of $E_2^* = 10E_2$ is utilized in the analytical model. The order of magnitude increase in stiffness is an estimate; further increases do not significantly influence results. By choosing a slightly skewed, but nearly hexagonal type II element, an upper use temperature densification event can be engineered between high and low CTE sublattices. When both adjacent unit cells and sublattices contact each other at the same ΔT, a nearly or completely densified and continuous structure can be formed.

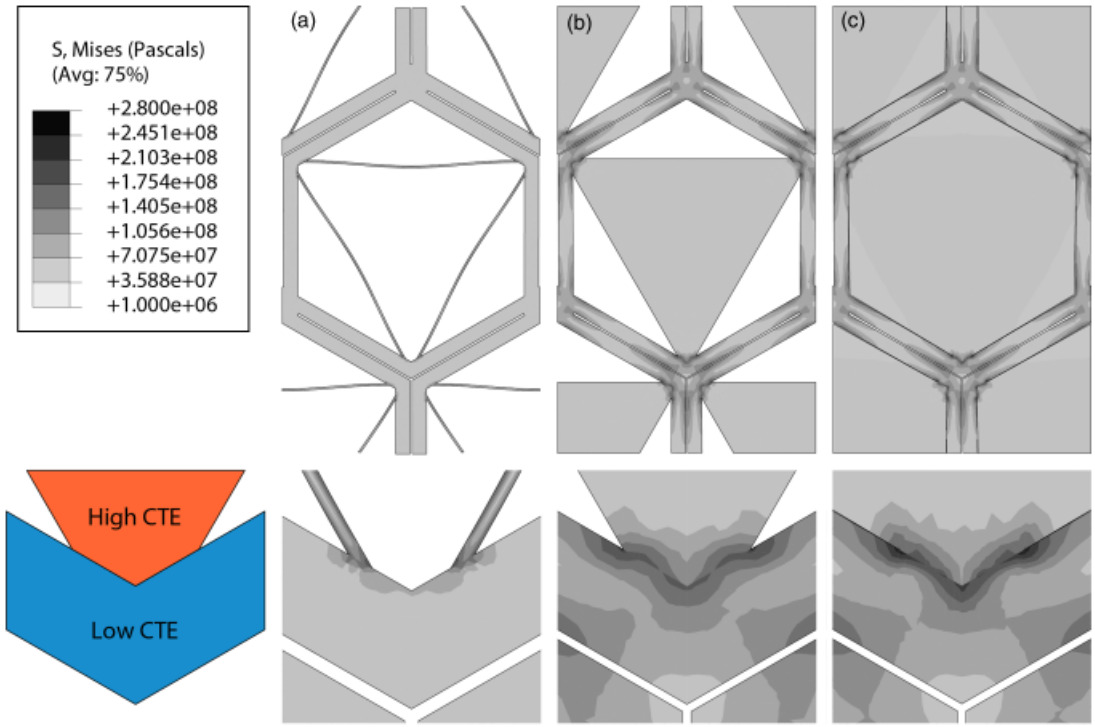

Fig. 9. Thermal stress distributions in Ti- and Al-fabricated lattice geometry with thin type I members (a), triangular type II member (b), and space-filling design (c).

The dovetail joint dimensions were chosen to maximize the effective length of type I members. Joint dimensions were minimized to reduce R_2 with practical consideration for the interface size and the need to maintain a robust mechanical connection between sublattices. Lattices previously investigated[5,7] used dovetail joints where the high CTE type II material composed the inner, male side of the connection. Additional material was added to the lattice at these locations to help facilitate a robust connection. This added material served to reduce the effective length of members resulting in a poorly predicted thermal response (Fig. 8). In the current design, the inner male component is now composed of the low CTE type I material, and the bimaterial joint is relocated to be enclosed in the inner type II member. Switching the low CTE material to the male side reduces thermal stresses resulting from the expansion of the high CTE material, which was previously confined by the low CTE constituent. It is hoped that plasticity can be avoided altogether with this configuration, in contrast to the previous dovetail joint design.

Fig. 10. Lattices of Ti alloy (struts) and Al alloy (hexagonal units) fabricated for measurement of the coefficient of thermal expansion.

The test specimen designed and fabricated in this work was chosen to have a skew angle of 30° and nearly space-filling inner type II member. By specifying the geometric parameters $w_1 = 3.0$ mm, $w_2 = 0.4$ mm, $\theta = 30°$, $H = 2.0$ mm, $S_r = 3.80$ mm, and unit cell length $L = 50.0$ mm, the designs in Fig. 10 are achieved. FE and analytical predictions for the geometries shown are listed in Table II.

(4) Lattice Fabrication

A metallic lattice was fabricated for CTE measurement purposes. The type I lattice was electro discharge machined from 3-mm-thick sheets of Ti–6Al–4V. The type II members were machined from 7075-T6 aluminum alloy. Sublattices were press-fit together. Tolerances were such that assembly with hand pressure was possible; however, a mechanical press was used to ensure proper assembly. The structure consists of 10 unit cells arranged so that two cells in the interior are separated from the edge by another unit cell to minimize edge effects (Fig. 10).

(5) CTE Measurement Methodology

Thermal expansion measurements on the Ti and Al lattice were performed using a two-dimensional (2D) digital image correlation (DIC) system. A high contrast black and white speckle pattern was applied using spray paint. Lattices were heated on a laboratory hot plate (Wensco, model #H1818RA4000) at a rate of 60°C/h from room temperature to 220°C. A frame of

Table II. Analytical and FE CTE Predictions for Thin, Triangular, and Hexagonal Type-2 Member Lattices Pictured in Fig. 9

Coefficient of thermal expansion (ppm/°C)	Thin	Triangular	Hexagonal	Fabricated
Analytical prediction	2.6	−1.4	−1.4	−1.4
Finite element	1.4	−1.6	−1.6	−1.1

Constituent properties and FE results are temperature average values from Table 1b from 20° to 70°C. Thin Type-2 members elastically buckled under compression for larger temperature excursions.

common silica insulation, approximately 1.5 in thick, was placed around the lattice with a glass plate on top. The temperature was recorded by four self-adhering K-type thermocouples (Omega, model SA1XL-K-SRTC, Omega Engineering Inc., Stamford, CT) located on the upper face of the lattice, two each on Ti and Al. Acetone was used to remove the applied paint at the location of the thermocouple attachments to increase heat transfer. The temperature of the lattice was taken to be the average of the four. Digital images were captured by CCD camera (AVT Dolphin F-201B, Allied Vision Technologies, Newburyport, MA) with a zoom lens (Tamron AF 70-300 1:4-5. 6, Tamron USA Inc., Commack, NY) positioned approximately 2 m from the specimen. The focal length was maximized subject in the confines of the laboratory space to minimize the effect of out of plane deformations on in-plane measurements. Images were taken every 5 s to record deformations. Two 300 W incandescent lights in hoods were positioned close above the glass plate for imaging purposes. Using the Vic-2D (Correlated Solutions, Correlated Solutions Inc., Columbia, SC) software, virtual extensometers placed on the reference image, and tracked through the images, measured the displacement between pairs of pixel subsets. A typical area of interest consisted of one unit cell with three Type D nodes visible. Strains were calculated from the relative displacement between pairs of subsets that were typically 23^2 pixels. Strains were measured in the Al and Ti and were calculated as the average of six virtual extensometers. Lattice strains were calculated as the average of three virtual extensometers placed between the three Type D nodes surrounding an interior unit cell. Temperature average CTE was measured by linear fitting to strain–temperature plots, where the average CTE over the temperature range is the slope of the resulting straight line. Extensometers were placed upon relatively unstressed material regions to measure the CTE of the constituents.

Image distortion from convective currents emanating from the specimen is a common problem when using DIC to record thermomechanical strains. A frame of silica fiber insulation was placed around the lattice and a glass plate on top to help thermally isolate the specimen from the camera. A fan is used to mix the air directly above the glass plate and carry hot air away from the lights.

(6) CTE Results

A typical experimental strain versus temperature plot is shown in Fig. 11 along with FE prediction. Temperature average CTE for the lattice and the constituent materials is reported in Table III. Although the DIC software is capable of measuring microstrains, scatter on the order of 1000 microstrain was present in the measurements due to image distortion. Convective currents emanating from the lighting were sufficient to cause visible inhomogeneous lensing in successive images. Measurements on the Ti were limited to the Type D joints resulting in short gauge lengths and larger scatter.

The average value of CTE for the constituent materials is measured to be ~4% higher than reported values (24.3 ppm/C for Al, and 9.4 ppm/C for Ti) (Table Ia), but are within experimental error. The lattice has an average measured CTE

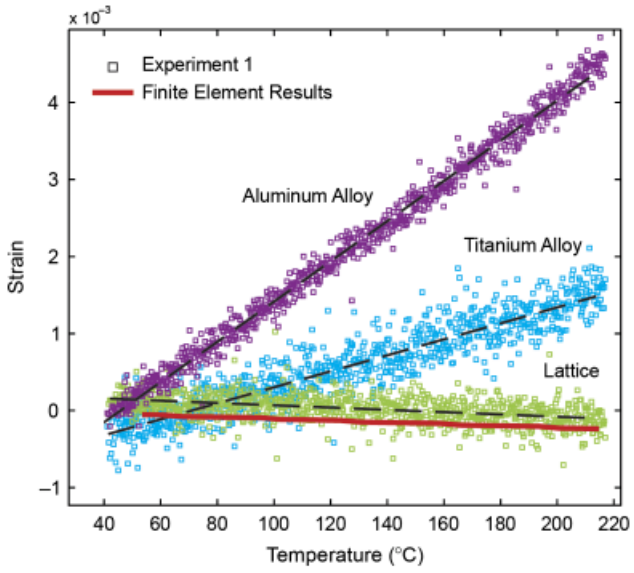

Fig. 11. Thermal strains measured in Al alloy, Ti alloy, and the lattice. Significant scatter in Ti measurements is due to the relatively short gauge lengths that had to be used.

of −0.9 ppm/C that is well predicted by FE of −1.1 ppm/C, and close to the analytical prediction of −1.4 ppm/C.

3.7 Discussion—Thermal Expansion

Measured thermal expansions of the lattice agree well with analytical and FE predictions. Differences between measured and FE prediction are believed to be due to the reduced effective length of the type I members resulting from fabrication imperfections causing premature contact between sublattices. The hexagonally shaped aluminum members had visible machining imperfections on some edges where they were cut from stock. The small wing-shaped gap between high and low CTE members results in a structure that is more imperfection sensitive than a lattice with triangular or prismatic beam-type members. Geometric imperfections in this gap can cause sublattices to impact each other before the predicted upper use temperature, reducing the effective length of type I members and driving up the CTE. Space-filling lattices with these features, such as aerodynamic surfaces, may be adversely affected by debris in these small gaps.

No plasticity is predicted in the revised dovetail geometry. The limited plasticity present in other designs[7] was a function of the bimaterial joint geometry used and is not inherent to the functional mechanics of the lattice itself.

Scatter in CTE measurements results from several sources. Convective currents in the air column between the specimen and the camera distort images through their associated density gradients and lensing effects.[12] Efforts were made to mitigate convective currents coming from the specimen and hotplate, but the incandescent lighting used for imaging proved a sufficient source of interference. A cold light source or a camera orientation that minimizes the effect of convective currents, by positioning it outside the affected area, would reduce the effect. The large scatter in the CTE measurements for Ti is due to the lattice geometry studied, the size of the unit cells, and the short lengths of relatively unstressed material available for measurements taken in the Type D node region.

The analytical model developed in Section II does a good job of predicting lattice thermal expansion. The model uses the simple assumption that the thermal expansion of the type II joint region is a weighted average of the constituent materials (Eq. (21)). In reality, a distinct material interface exists between the constituents, and the thermal response is much more complicated. The analytical CTE prediction of −1.4 ppm/C for the lattice is close to the FE predicted value of −1.1 ppm/C and

Table III. Measured CTE of Lattices and Constituent Materials (95% Confidence Bounds), and FE Prediction for Lattice using Measured Values (ppm/°C)

	Aluminum (measured)	Titanium (measured)	Lattice (measured)	FE prediction
Exp. 1	26.1 (25.9–26.3)	10.4 (10.0–10.7)	−1.5 (−1.7 to −1.3)	−0.8
Exp. 2	24.9 (24.7–25.1)	10.0 (9.6–10.7)	−0.8 (−0.9 to −0.6)	−0.6
Exp. 3	25.5 (25.4–25.6)	9.1 (8.6–9.6)	−0.6 (−0.7 to −0.5)	−2.6
Exp. 4	24.9 (24.8–25.0)	9.1 (8.7–9.5)	−0.8 (−0.8 to −0.6)	−2.2
Average	25.4	9.7	−0.9	−1.3

sufficiently accurate to help characterize the design space to locate geometries of interest.

CTE measurements performed on a titanium and aluminum lattice using 2D DIC were able to validate the analytical and FE predictive models used in its design. The metal lattice behaved elastically over a temperature range of 175°C, exhibiting consistent negative thermal expansion. The design space identified through the analytical model suggests the ability to realize a family of structures with a wide range of stiffness and thermal expansion properties.

IV. Stiffness

(1) Basic Stiffness Results for Pin-Jointed Lattices

(A) Elastic Properties: The unit cell of the design without spacers, shown in Fig. 12(a), is loaded by a set of forces, parameterized by P, Q, and S. It is presumed that the lattice has been designed in the manner described above, such that the bending stiffness of struts of type I are very low, whereupon their behavior is stretch dominated. In such a situation, the lattice can be analyzed as if it were pin-jointed.

The resulting behavior is isotropic in the plane of the lattice, and stated as

$$\varepsilon_{xx} = \frac{\sigma_{xx}}{E} - \frac{\nu\sigma_{yy}}{E} + \alpha\Delta T \tag{27a}$$

$$\varepsilon_{yy} = \frac{\sigma_{yy}}{E} - \frac{\nu\sigma_{xx}}{E} + \alpha\Delta T \tag{27b}$$

$$\varepsilon_{xy} = \frac{\sigma_{xy}}{2G} \tag{27c}$$

where E, ν, G, and α are the in-plane Young's modulus, the Poisson ratio, shear modulus, and CTE, respectively, of the lattice.

The biaxial stiffness is the ratio of the biaxial stress to the in-plane strain under equibiaxial loading,[5] and can be deduced as

$$S_b = \frac{(\sqrt{3}\cos\theta - \sin\theta)^2}{2\sqrt{3}L_1\left[\frac{1}{E_1 w_1} + \frac{2\sin^2\theta}{3E_2 w_2}(\cos\theta + \sqrt{3}\sin\theta)\right]} \tag{28}$$

Note that this corrects a misprint in the previously published formula in Steeves *et al.*,[5] which is missing the leading 2 in the denominator. The shear modulus is

$$G = \frac{(\sqrt{3}\cos 2\theta + \sin 2\theta)^2}{8\sqrt{3}L_1\left[\frac{1}{E_1 w_1} + \frac{2\sin^2 2\theta}{3E_2 w_2}(\cos\theta + \sqrt{3}\sin\theta)\right]} \tag{29}$$

In these expressions for S_b and G, L_1 is used rather than L because L_1/w_1 is the aspect ratio of type I elements.

The Poisson ratio for the lattice may be computed from

$$\nu = \frac{S_b - 2G}{S_b + 2G} \tag{30}$$

and the Young's modulus

$$E = 2G(1+\nu) \tag{31}$$

Note that, in certain circumstances, the Poisson ratio will be zero or negative. For example, when $E_2 \gg E_1$, the Poisson ratio reduces to

$$\nu = \frac{\cos 2\theta - \sqrt{3}\sin 2\theta}{3 + 2(\sqrt{3}\cos\theta + \sin\theta)\sin\theta} \tag{32}$$

As a consequence, it is zero at $\theta = \pi/12$, and negative for $\theta > \pi/12$.

The introduction of a stiff spacer, as in Fig. 3, has no effect on the elastic properties of the lattice. If the spacer is a stiff component (e.g., composed of a solid plate rather than a set of truss or beam elements), the elastic properties of the lattice are still given by the values in Eqs. (28) and (29). This situation arises because for a stiff spacer, when we neglect its deformation and treat it as rigid, both stress and elastic strain scale in the same way with the size of the spacer. To show this for the case of equibiaxial stress, the loads in Fig. 12(b) are

$$P = (L + H)\sigma_B \tag{33a}$$

$$Q = \frac{\sqrt{3}}{2}(L + H)\sigma_B \tag{33b}$$

where σ_B is the applied biaxial stress. Because the spacers are rigid, the forces experienced by the adjacent nodes are the same. The stress are

$$\sigma_{11} = \frac{2Q}{\sqrt{3}L} \tag{34a}$$

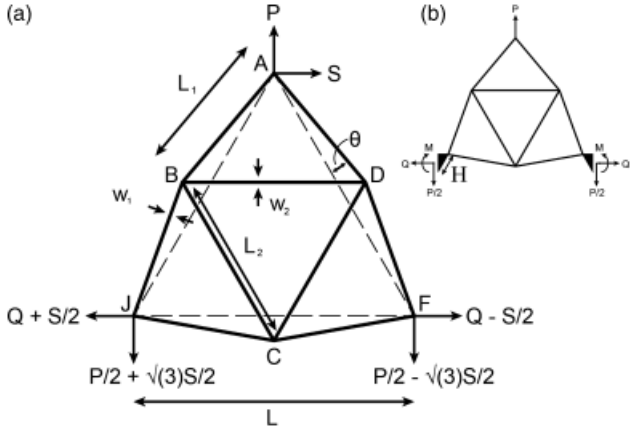

Fig. 12. Pin-jointed unit cell subject to loads P, Q, and S used in stiffness calculation (a). Spaced lattice unit cell with applied loads P and Q (b).

$$\sigma_{22} = \frac{P}{L} \tag{34b}$$

And the changes in dimensions of the lattice are

$$\Delta u_1 = \varepsilon_{11} L = \frac{1}{E}\left[\frac{2Q}{\sqrt{3}} - \nu P\right] \tag{35a}$$

$$\Delta u_2 = \varepsilon_{22}\frac{\sqrt{3}L}{2} = \frac{\sqrt{3}}{2E}[P - \nu Q] \tag{35b}$$

The strains are

$$\bar{\varepsilon}_{11} = \frac{\Delta u_1}{L + \mathrm{H}} \tag{36a}$$

$$\bar{\varepsilon}_{22} = \frac{2\Delta u_2}{\sqrt{3}(L + \mathrm{H})} \tag{36b}$$

Using Eqs. (30), (31), and (32), with (36), the strains become

$$\varepsilon_{11} = \varepsilon_{22} = \frac{1}{E}[\sigma_b - \nu\sigma_b] \tag{37}$$

showing that the strains are not a function of the size of the spacer.

For the case of shear loading for a lattice with spacer with an applied shear stress τ, the forces in Fig. 12(b) are

$$P = (L + H)\tau \tag{38a}$$

$$Q = \frac{-\sqrt{3}\,(L + H)\tau}{2} \tag{38b}$$

Because the spacer is rigid, the resulting macroscopic strains are

$$\bar{\varepsilon}_{11} = \frac{1}{E}\left[\frac{Q}{\frac{\sqrt{3}(L+H)}{2}} - \nu\frac{P}{L+H}\right] = \frac{1}{E}[-\tau - \nu\tau] \tag{39a}$$

$$\bar{\varepsilon}_{22} = \frac{1}{E}\left[\frac{P}{(L+H)} - \nu\frac{Q}{\frac{\sqrt{3}(L+H)\tau}{2}}\right] = \frac{1}{E}[\tau + \nu\tau] \tag{39b}$$

This indicates that there is no stiffness penalty upon introduction of a stiff spacer.

(2) In-Plane Compression Measurements

In-plane compression experiments have been used to generate stress/strain measurements. The objectives are two-fold: (i) allow calibration of the mechanical robustness and stiffness of representative lattices, and (ii) provide validation data for the ensuing FE calculations. For these purposes, it suffices to fabricate monolithic lattices from 1-mm-thick plates by laser cutting. To probe the yielding and strain-hardening characteristics, one set of lattices has been generated from 304 stainless steel. During testing, out of plane buckling was prevented by constraining the lattice between two 12.7-mm-thick tempered glass plates, bolted to an aluminum frame. The experiments were performed in an MTS™ 810 servohydraulic testing system under displacement control, using a displacement rate of 0.5 mm/min. Images of the lattice were recording every 15 s during the tests using a CCD camera connected to an image correlation system.

Two different type II member geometries were used. The stress–strain behaviors, shown in Fig. 14, reveal robust behavior, characterized by yielding followed by strain hardening. In all cases, yielding occurs in the type I members at critical stress levels in the range, $15 \le \sigma_c \le 18$ MPa. The bright regions in the images (Fig. 13) indicate the occurrence of out-of-plane plastic buckling. Unload–reload measurements reveal hysteresis and decreasing stiffness with increase in plastic strain.

(3) Experimental and FE Results

Stress strain curves generated from FE modeling (FEM) are plotted alongside experimental results in Fig. (14). The 304 stainless steel was modeled by linear elastic response followed by yielding with isotropic hardening. Twenty node biquadratic elements (C3D20R) were used in these calculations. Homogeneous strains were applied to the RVE in two directions. The influence of the glass plates used to confine specimens out of plane was not modeled.

Notable features of the experimental stress–strain curves include a reduction in elastic stiffness with increasing strain past initial yield as evident in the unload–reload regions, and significant hysteresis in these regions. No reduction in stiffness is seen in models restricted to in-plane deformations. Models seeded with imperfections to initiate buckling show the same reduction in stiffness with strain as experiments. Frictional interactions between the lattices and the glass plates used to constrain out-of-plane motion are attributed as the source of hysteresis observed in the experiment. The collapse modes, plastic buckling of type I members oriented most obliquely to the loading direction, and out-of-plane plastic hinging in the same yielded members are accurately captured by the FE results (Fig. 15).

(4) Comparison of Pinned and Bonded Stiffness

To compare pin-jointed analytical and FE-bonded predictions for stiffness, the equations in Section II were used to identify lattice geometries with zero thermal expansion and maximum stiffness. For a given skew angle θ and lattice unit cell length L, Eq. (17) can be used to identify values of w_1 and w_2 that produce maximum stiffness for a given pair of constituent materials. Using the temperature-average properties of Ti and Al (Table Ia), a variety of zero CTE lattices as predicted by Eq. (17) are identified (Fig. 16). The associated aspect ratio of type I members, $\hat{L}_1/w_1$, decreases with increasing skew angle from 20.4 to 5.0 (Figs. 16(a–d)). The stiffness of the analogous pin-jointed structures, those having the same member dimensions, is plotted along with FEM results in Fig. 17, where $V_{f,i}$ is the fraction of solid material of type i.

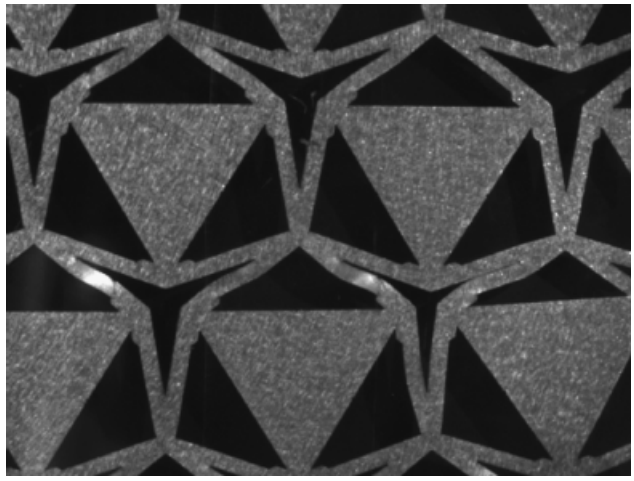

Fig. 13. The 304 stainless steel lattice compressed along the vertical axis. Bright areas indicate out-of-plane deformation associated with member buckling.

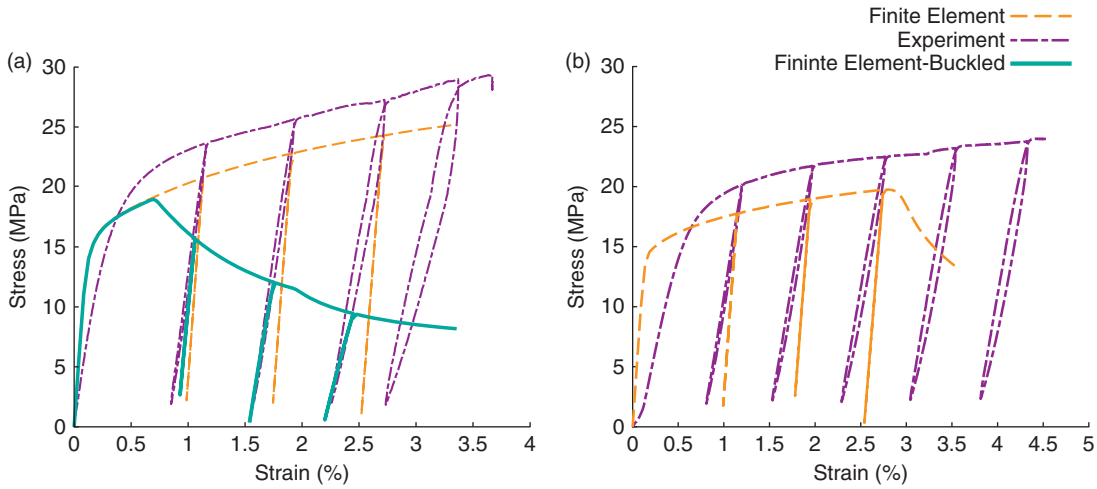

Fig. 14. Uniaxial compression strain–stress behavior or 304 Steel lattices. (a) Triangular type II element. (b) Thin type II members.

(4) Discussion—Stiffness

Experimental and FE results for 304 steel lattices in axial compression show that the geometries tested are prone to out-of-plane deformations, suggesting relatively good in-plane properties. FE analysis of an RVE shows good agreement with experiments conducted on steel lattices. To avoid the complex loading interactions between glass plates used to confine test specimens, thicker lattices not prone to out-of-plane plane deformations should be tested. Lattices incorporated into other structures and attached at nodal locations will have reduced out-of-plane degrees of freedom, such as when they are used as the face sheet in a sandwich panel, and will also be less prone to buckling in this manner. Additional boundary conditions or structural elements within the RVE technique can be used to model the behavior of more confined lattices.

Analytical models for pin-jointed biaxial stiffness and CTE give results that are similar to those from FE analysis of bonded lattices with slender members. Bonded lattices have increased CTE and stiffness over analytical predictions at higher relative densities. Decreasing member slenderness causes more overlap of members near joints leading to potentially larger deviations from the assumptions in Section II regarding the thermomechanical response of the joint region. Beam theory cannot accurately predict the deformation of members with aspect ratios less than about 10; in this case, Ti and Al lattices with $\theta > \sim 26^{\circ}$. However, the associated geometries still have a CTE very close to the value predicted by Eq. (26). Stress distributions in lattices subjected to equibiaxial tensile straining show greater uniformity at lower relative densities suggesting more efficient and stretch-dominated behavior. The stiffness of the pin-jointed lattice is clearly recovered in bonded lattices with slender members as predicted in Section II.

IV. Concluding Remarks

Modifications to the geometry and modeling assumptions of previous bonded lattice designs of the UCSB lattice have resulted in a design scheme capable of rapidly identifying geometries that inherit the CTE and stiffness properties of the parent pin-jointed structure. The pin-jointed structure has been shown to be near optimal in stiffness over a wide range of densities.[4] Similar bonded lattices have obvious advantages in terms of fabricability. The behavior of these lattices is elastic and

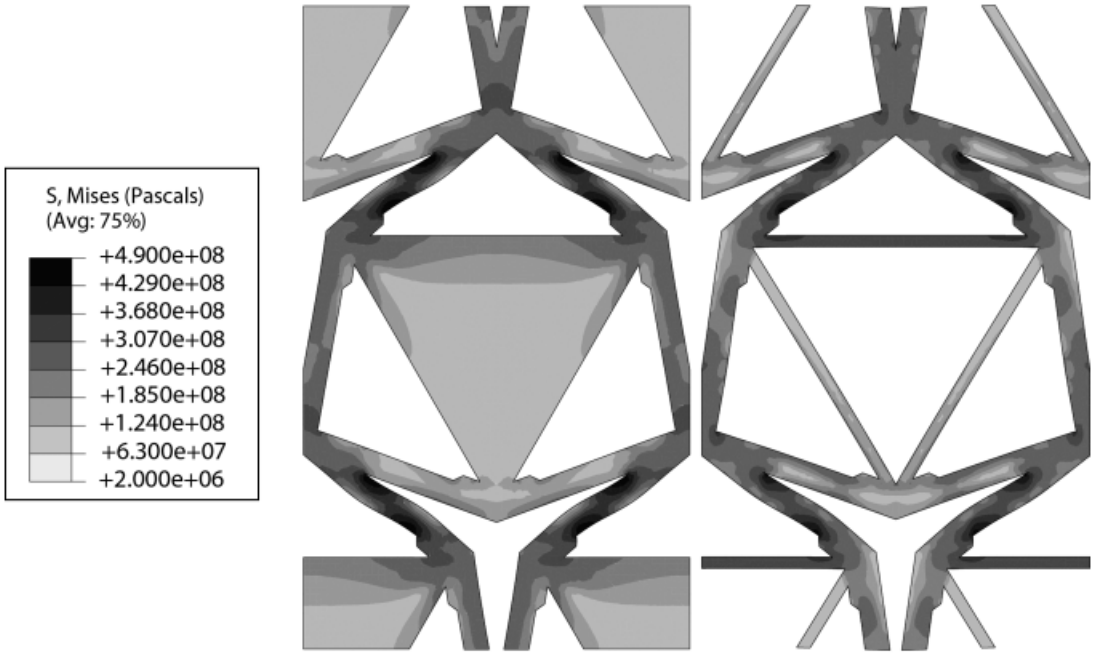

Fig. 15. Finite-element stress distributions in uniaxially compressed 303 stainless steel lattices. Yielding occurs in struts linking triangle vertices to six-member joints and involves out-of-plane displacements. This behavior agrees well with experimental results.

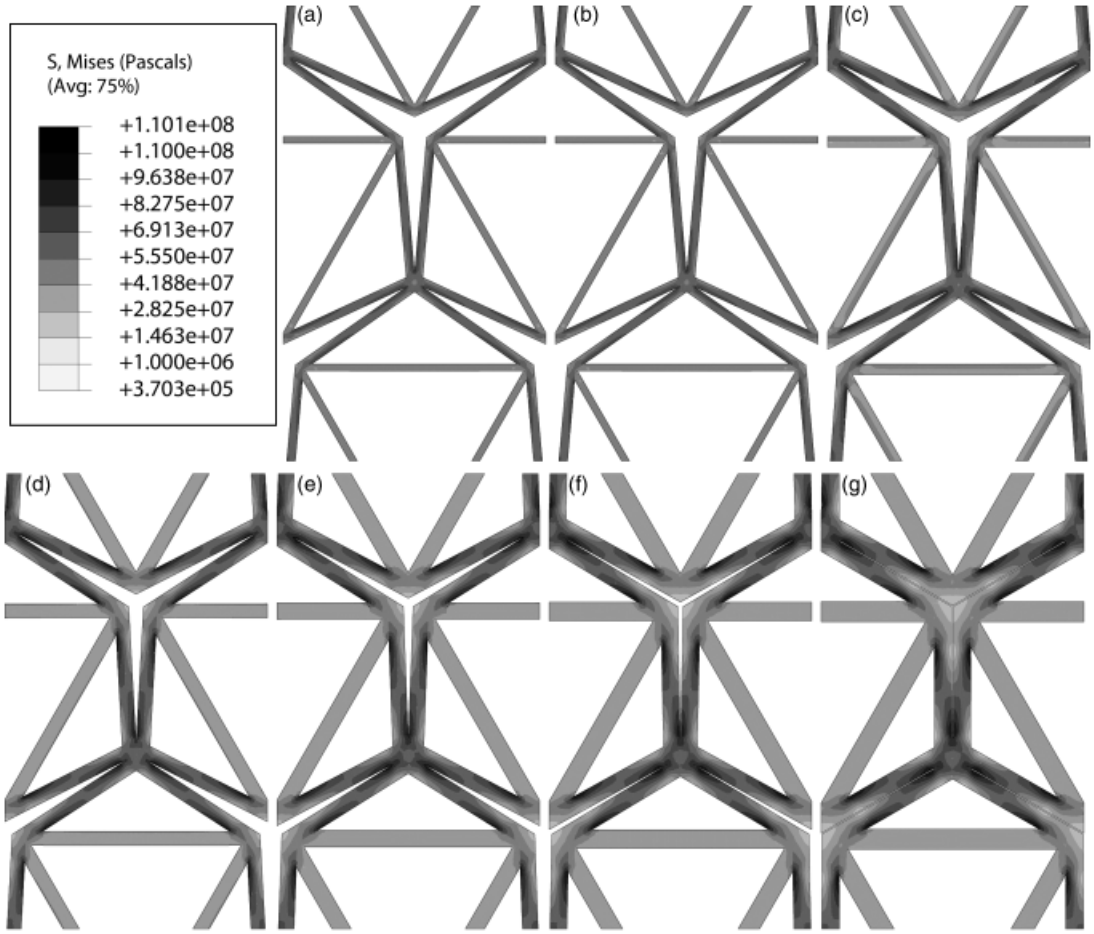

Fig. 16. Stress distributions in lattices made from Ti alloy and Al alloy with maximum biaxial stiffness as predicted by the pin-jointed analytical model, subject to 0.1% biaxial tensile strain. Skew angles range from 24.5° to 30° and volume fractions of solid from 14% to 46% (a–g). Stress distributions become more uniform with increasing slenderness moving toward behavior similar to the pin-jointed response.

amenable to fabrication on length scales ranging from aerospace structures to those relevant to nanotechnology.

The behavior of the bonded structure tends toward that of the pin-jointed lattice at lower relative densities in maximum stiffness lattices having slender members. At higher densities, lattice members have aspect ratios too low for beam-theory-based models to accurately predict their behavior. CTEs in these structures are still significantly different from the mean of the constituents. Three-dimensional computer-aided design and FE can be used to identify and fabricate rigid-jointed lattices with a tailored thermal expansion coefficient that is well predicted by modeling.

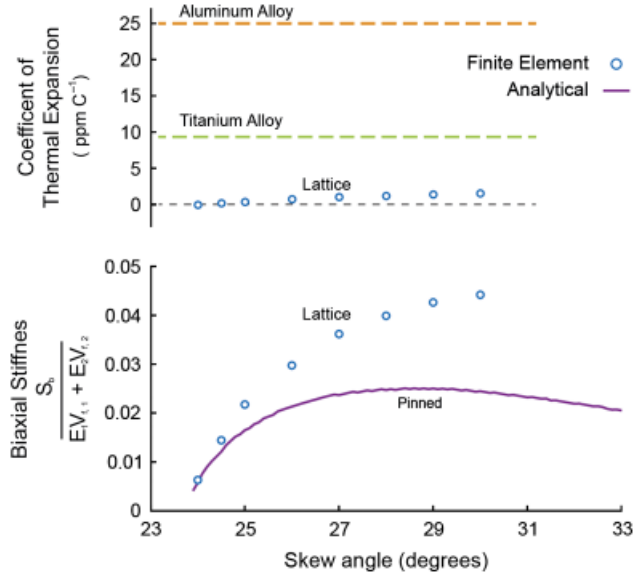

Fig. 17. Results for the coefficient of thermal expansion and biaxial stiffness for lattices shown in Fig. 16. Analytical results derived from a pin-jointed model are shown as are results from finite-element analysis of lattices having bonded joints.

A lattice composed of Ti–6Al–4V and 7075-T6 Al was designed, fabricated, and measured to have a negative thermal expansion coefficient. Design space illustrated by the analytical model developed in this work shows the possibility for realizing material systems with a wide range of CTE including significantly negative thermal expansions. Such negative CTE materials can be used in a limited capacity in systems composed mostly of more conventional positive CTE materials, so that the system average is zero or low. The demonstrated ability of this design approach opens the door for the investigation and application of a wide family of materials with novel properties including high stiffness and low thermal expansion.

Further extension of these analytical and numerical techniques can be used to investigate the introduction of anisotropy by allowing geometry to vary among members of the same type in a unit cell allowing properties to be tailored in two directions. Rapid prototyping and other direct fabrication techniques can be used to fabricate volumetric lattices with properties tailored in three dimensions. The analytical and FE techniques can be extended to consider these variations.

Possible combinations lattice constituent materials include ceramics, glasses, and glass ceramics. In high-temperature applications, the thermal strains in these materials can be tailored to match the thermal strains experienced in significantly cooler

supporting substructures. A low CTE glass, such as Zerodur, used as the type I material will offer a large CTE ratio, λ, when paired with a wide range of other higher expansion materials making available a wide range of achievable CTE (Fig. 5).

Other considerations exist in the design of these systems. These include (i) transient heating effects resulting from mismatches in thermal conductivity between constituents and nonuniform heating, (ii) the net CTE of the lattice is a function of the relative thermal strain between sublattices that may be varying due to transients and inhomogeneous thermal loading, which can affect the response, and (iii) aerodynamic surfaces are often curved surfaces so that nonflat shapes with a tailored thermal expansion coefficient may be desired. The techniques developed and exercised in this paper can be extended to address these issues, and the strength and failure modes of systems can also be addressed.

References

[1]R. S. Lakes, "Cellular Solid Structures with Unbounded Thermal Expansion," *J. Mater. Sci. Lett.*, **15**, 475–7 (1996).

[2]O. Sigmund and S. Torquato, "Composites with Extremal Thermal Expansion Coefficients," *Appl. Phys. Lett.*, **69**, 3203–5 (1996).

[3]L. V. Gibiansky and S. Torquato, "Thermal Expansion of Isotropic Multiphase Composites and Polycrystals," *J. Mech. Phys. Solids*, **45**, 1223–52 (1997).

[4]G. Jefferson, T. A. Parthasarathy, and R. J. Kerans, "Tailorable Thermal Expansion Hybrid Structures," *Int. J. Solids Struct.*, **46**, 2372–87 (2009).

[5]C. A. Steeves, S. L. Lucato, M. Y. He, E. Antinucci, J. W. Hutchinson, and A. G. Evans, "Concepts for Structurally Robust Materials that Combine Low Thermal Expansion with High Stiffness," *J. Mech. Phys. Solids*, **55**, 1803–22 (2007).

[6]J. N. Grima, P. S. Farrugia, R. Gatt, and V. Zammit, "A System with Adjustable Positive or Negative Thermal Expansion," *Proc. R. Soc. A*, **463**, 1585–96 (2007).

[7]C. A. Steeves, C. Mercer, E. Antinucci, M. Y. He, and A. G. Evans, "Experimental Investigation of the Thermal Properties of Tailored Expansion Lattices," *Int. J. Mech. Mater. Des.*, **5**, 195–202 (2009).

[8]M. Danielsson, D. M. Parks, and M. C. Boyce, "Three-Dimensional Micromechanical Modeling of Voided Polymeric Materials," *J. Mech. Phys. Solids*, **50**, 351–79 (2002).

[9]K. Bertoldi, Harvard University, School of Engineering and Applied Sciences (discussion).

[10]Simulia. *ABAQUS 6.9-EF*. Simulia, Providence, RI, 2009.

[11]Mathworks. *MATLAB 2008b*. Mathworks, Natick, MA, 2008.

[12]M. A. Sutton, J. J. Orteu, and H. W. Schreier, *Image Correlation for Shape, Motion and Deformation Measurements*. Springer, Berlin, 2009. □